



On vibration analysis of functionally graded carbon nanotube reinforced magneto-electro-elastic plates with different electro-magnetic conditions using higher order finite element methods



M. Vinyas ^{a,*}, D. Harursampath ^a, S.C. Kattimani ^b

^a Nonlinear Multifunctional Composites Analysis and Design (NMCAD) Laboratory, Department of Aerospace Engineering, Indian Institute of Science, Bangalore, 560012, India

^b Department of Mechanical Engineering, National Institute of Technology Karnataka, Surathkal, 575025, India

ARTICLE INFO

Article history:

Received 19 January 2020

Received in revised form

29 February 2020

Accepted 23 March 2020

Available online 8 April 2020

Keywords:

Carbon nanotube

Magneto-electro-elastic

Higher order shear deformation theory

Coupled frequency

Electro-magnetic conditions

ABSTRACT

This article deals with evaluating the frequency response of functionally graded carbon nanotube reinforced magneto-electro-elastic (FG-CNTMEE) plates subjected to open and closed electro-magnetic circuit conditions. In this regard finite element formulation has been derived. The plate kinematics adjudged via higher order shear deformation theory (HSDT) is considered for evaluation. The equations of motion are obtained with the help of Hamilton's principle and solved using condensation technique. It is found that the convergence and accuracy of the present FE formulation is very good to address the vibration problem of FG-CNTMEE plate. For the first time, frequency response analysis of FG-CNTMEE plates considering the effect of various circuit conditions associated with parameters such as CNT distributions, volume fraction, skew angle, aspect ratio, length-to-thickness ratio and coupling fields has been carried out. The results of this article can serve as benchmark for future development and analysis of smart structures.

© 2020 China Ordnance Society. Production and hosting by Elsevier B.V. on behalf of KeAi Communications Co. This is an open access article under the CC BY-NC-ND license (<http://creativecommons.org/licenses/by-nc-nd/4.0/>).

1. Introduction

In the recent years, many researchers have revealed that carbon nanotubes (CNTs) exhibit pronounced mechanical properties as opposed to continuous carbon fibers. Also, CNTs when embedded in polymer matrix provides exceptional elastic modulus and strength which has made them to evolve as a potential candidate for various engineering applications. On the other hand, the concept of functionally graded materials (FGMs) has revolutionised the engineering domain with its vast versatility. More importantly, it effectively counters the problems witnessed in sandwich structures such as stress concentration, delamination, matrix cracks etc and enhances the structural performance. The tremendous

impact made by CNTs and FGMs individually has motivated many pioneers to come up with functionally graded carbon nanotube-reinforced composites (FG-CNTRC) and evaluate its mechanical and structural performance.

The nonlinear vibration response of FG-CNTRC plates was assessed by Wang et al. [1,2] and Kaci et al. [3]. Liew et al. [4] evaluated both the linear and nonlinear behaviour of FG-CNTRC structures under influence of thermo-mechanical environment. Similarly, the influence of thermal loads on the vibration behaviour of FG-CNTRC plates was investigated by George et al. [5] with the aid of FE methods. Selim et al. [6] and Lei et al. [7,8] explored the element-free kp-Ritz method to understand the free vibration behaviour of FG-CNTRC plates. Through layer-wise approach, the structural response of FG-CNTRC was probed by Kumar et al. [9]. The frequency response of FG-CNTRC plates was examined by Phung-Van et al. [10] under the framework of isogeometric analysis. Zhu et al. [11] examined the frequencies of FG-CNTRC plates employing first order shear deformation theory (FSDT) in conjunction with finite element (FE) methods. Duc et al. [12]

* Corresponding author. Department of Aerospace Engineering, Indian Institute of Science (IISc), Bangalore, India, 560012.

E-mail addresses: vinyasmahesh@iisc.ac.in, vinyas.mahesh@gmail.com (M. Vinyas).

Peer review under responsibility of China Ordnance Society

investigated the influence of elastic foundations on the free vibrations of FG-CNTRC plates using FSDT. Analogously, using FSDT as kinematic model, Malekzadeh et al. [13] and Kiani et al. [14] carried out free vibration analysis through differential quadrature method (DQM) and Ritz method, respectively. Using similar approach of Ritz method, the influence of skew angles [14] and cut-outs [15,16] on vibrations of FG-CNTRC plates was demonstrated by Kiani and co researchers. The dynamic characteristics of CNTRC beams was assessed by Lin et al. [17] and the results were compared between FSDT and higher order shear deformation theory (HSDT). The vibration analysis of FG-CNTRC plates with different shapes was performed by Zhang et al. [18,19] through element free IMLS Ritz method and by Fantuzzi et al. [20] through non-uniform rational B-splines (NURBS) curves using generalized differential quadrature (GDQ) method. It is known that in order to properly define the displacement fields for thick plates, HSDT is more opt than FSDT. Additionally, HSDT enhances the computational efficiency and eliminates the requirement of shear correction factor [21–28]. Consequently, the governing equations based on the HSDT emerged to analyze FG-CNTRC structures. Natarajan et al. [29] investigated the natural frequencies of sandwich plates embedded with FG-CNTRC facesheets. Mehar et al. [30] developed a FE model to assess the vibration behaviour of FG-CNTRC plates on the basis of HSDT.

The developments in the field of smart materials also have made it feasible to unite the benefits of multifunctionality with structural robustness and adaptability. One such category is magneto-electro-elastic (MEE) smart structures where energy interactions between magnetic, electric and elastic phases can be witnessed. This has led to the replacement of many conventional materials in applications such as nano-electromechanical systems (NEMS), nano-probes, atomic force microscope (AFM), nano-actuators and nano sensors. Therefore, it is very crucial to assess the associated electromagnetism phenomenon either experimentally or with the aid of sophisticated computational techniques [31–35]. Many literatures have focused on unveiling the various coupled characteristics of functionally graded magneto-electro-elastic (FGMEE) structures. Few are summarised here for the benefit of the readers. Pan and Han [36] examined the free vibrations of exponentially graded MEE plates. Ramirez et al. [37] assessed the frequency response of FGMEE plates. Considering plane stress state, the structural response of FGMEE beams was analytically studied by Huang et al. [38]. Through finite element (FE) procedure, Bhangale and Ganesan [39] investigated the free vibration behaviour of FGMEE plates. Milazzo [40,41] developed two-dimensional refined equivalent single layer models and studied the dynamic response of FGMEE plate in detail. The effect of internal crack on the dynamic performance of FGMEE structures was probed by Feng and Su [42]. Vinyas et al. [43–46] derived a FE formulation and demonstrated the vibration control abilities of various kinds of MEE skew plates treated with active constrained layer damping. Also, through the sensitivity analysis [47] the performance optimization of MEE structures can also be achieved effectively. Wu et al. [48] demonstrated the wave propagation characteristics in FGMEE plates. Wu and Tsai [49] proposed modified Pagano method to assess the dynamic behaviour of FGMEE plate subjected to closed-circuit condition. Hou and Leung [50] addressed the transient response problem of MEE hollow cylinders through orthogonal expansion technique. Bhangale and Ganesan [51] analysed the frequency response of FGMEE cylindrical shells. Among the static analysis, Wu and Tsai [52] in their work adopted an asymptotic approach and evaluated the influence of various forms of loading on the static response of doubly curved FGMEE shells. Li et al. [53] investigated the effect of uniform load on FGMEE circular plate. Sladek et al. [54] evaluated the bending response of FGMEE circular plate by employing a meshless method.


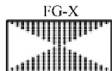
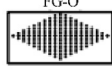

Vinyas and co-researchers designed stepped functionally graded magneto-electro-elastic (SFG-MEE) structures and their static behaviour was analysed under different working environments [55–61]. Very recently, Mohammadimehr et al. [62] reported on free vibration of CNTMEE cylindrical shell using FSDT. Also, with the recent development in technology, the machine learning techniques can also be adopted for accurate and effective analysis of MEE structures in the near future [63–65].

The extensive literature review suggests that the structural assessment of CNTMEE structures is still an over-looked area which requires more attention. Alongside, the opportunities to collectively exploit the benefits of FG-CNTs, MEE material, FE methods and kinematics accuracy of HSDT have motivated the authors to take up this current work. The coupled response of the MEE smart structure is significantly influenced by the applied magnetic and electric constraints. Hence this works makes the first attempt to study the influence of open and closed circuit electromagnetic boundary conditions associated with different parameters, on the frequency response of FG-CNTMEE plates under the framework of FE methods. The C^1 continuity requirement of HSDT is fulfilled by considering second order derivative terms as higher order rotational degrees of freedom. Therefore, its computational efficiency is found to be better than the numerical software in terms of computational time and costs. The equations of motion are developed by using Hamilton's principle and HSDT which are solved by incorporating condensation technique. A detailed evaluation of various parameters such as CNT distribution, CNT volume fraction, piezoelectric matrix material, skew angle, coupling fields, aspect ratio (a/h), the length-to-width ratio (a/b) has been carried out.

2. Materials and methods

The present work considers MEE composite plate made of carbon nanotubes (CNTs) reinforced in piezoelectric matrix. Here, CNTs act as piezomagnetic fibers. Apart from uniformly distributed (UD) CNTs, this work also considers various functionally graded CNT distribution patterns such as FG-X, FG-O and FG-V whose graphical and mathematical equations are illustrated in Table 1. Through the rule of mixture, the effective properties of FG-CNTMEE material are estimated as follows [15]:

Table 1
CNT distribution with corresponding mathematical expression.

CNT distribution	Mathematical expression Kiani [15]	Pictorial representation
UD	$V_{CNT} = V_{CNT}^*$	
FG-X	$V_{CNT} = \frac{4 z }{h} V_{CNT}^*$	
FG-O	$V_{CNT} = 2 \left(1 - \frac{2 z }{h} \right) V_{CNT}^*$	
FG-V	$V_{CNT} = \left(1 + \frac{2 z }{h} \right) V_{CNT}^*$	

where, $V_{CNT}^* = \frac{w_{CNT}}{w_{CNT} + (\rho_{CNT}/\rho_m) - (\rho_{CNT}/\rho_m)w_{CNT}}$ and w_{CNT} represents mass fraction of CNT.

$$E_{11} = \eta_{11} V_{\text{CNT}} E_{11}^{\text{CNT}} + V_m E^m, \quad \frac{\eta_2}{E_{22}} = \frac{V_{\text{CNT}}}{E_{22}^{\text{CNT}}} + \frac{V_m}{E^m}, \quad \frac{\eta_3}{G_{12}} = \frac{V_{\text{CNT}}}{G_{12}^{\text{CNT}}} + \frac{V_m}{G^m}, \quad v_{12} = V_{\text{CNT}} v_{12}^{\text{CNT}} + V_m v^m \rho = V_{\text{CNT}} \rho^{\text{CNT}} + V_m \rho^m \quad (1)$$

Where, E , G , ρ and v denote the elastic modulus, shear modulus, density and Poisson’s ratio respectively. The superscripts CNT and m represents corresponding values for CNT fiber and piezoelectric matrix, respectively.

V_{CNT} and V_m represent CNT and matrix volume fractions, respectively. Meanwhile, η_1, η_2 and η_3 are CNT/matrix efficiency parameters which are determined by molecular dynamics simulation.

The coupled constitutive equation of FG-CNTMEE material can be represented as follows [23]:

$$\{\sigma\} = [C]\{\varepsilon\} - [e]\{E\} - [q]\{H\} \{D\} = [e]^T\{\varepsilon\} + [\eta]\{E\} + [m]\{H\}\{B\} = [q]^T\{\varepsilon\} + [m]\{E\} + [\mu]\{H\} \quad (2)$$

where, $[C]$, $[e]$, $[q]$, $[m]$, $[\eta]$ and $[\mu]$ are the elastic stiffness, piezoelectric, magnetostrictive, electromagnetic, dielectric and magnetic permeability coefficient matrices, respectively. Also, $\{\sigma\}$, $\{D\}$ and $\{B\}$, represent the stress tensor, electric displacement and the magnetic flux, respectively; $\{\varepsilon\}$, $\{E\}$ and $\{H\}$ are the linear strain tensor, electric field and magnetic field, respectively.

$$\{\varepsilon_b\} = \begin{Bmatrix} \varepsilon_x \\ \varepsilon_y \\ \gamma_{xy} \end{Bmatrix} = \begin{bmatrix} \frac{\partial}{\partial x} & 0 & 0 \\ 0 & \frac{\partial}{\partial y} & 0 \\ \frac{\partial}{\partial y} & \frac{\partial}{\partial x} & 0 \end{bmatrix} \begin{Bmatrix} u_0 \\ v_0 \\ w_0 \end{Bmatrix} + (z + c_1 z^3) \begin{bmatrix} \frac{\partial}{\partial x} & 0 \\ 0 & \frac{\partial}{\partial y} \\ \frac{\partial}{\partial y} & \frac{\partial}{\partial x} \end{bmatrix} \begin{Bmatrix} \theta_x \\ \theta_y \end{Bmatrix} + c_1 z^3 \begin{bmatrix} \frac{\partial}{\partial x} & 0 \\ 0 & \frac{\partial}{\partial y} \\ \frac{\partial}{\partial y} & \frac{\partial}{\partial x} \end{bmatrix} \begin{Bmatrix} \kappa_x \\ \kappa_y \end{Bmatrix} \quad (6)$$

$$\{\varepsilon_s\} = \begin{Bmatrix} \gamma_{xz} \\ \gamma_{yz} \end{Bmatrix} = \begin{bmatrix} 0 & 0 & \frac{\partial}{\partial x} \\ 0 & 0 & \frac{\partial}{\partial y} \end{bmatrix} \begin{Bmatrix} u_0 \\ v_0 \\ w_0 \end{Bmatrix} + \begin{bmatrix} 1 & 0 \\ 0 & 1 \end{bmatrix} \begin{Bmatrix} \theta_x \\ \theta_y \end{Bmatrix} + c_2 z^2 \begin{bmatrix} 1 & 0 \\ 0 & 1 \end{bmatrix} \begin{Bmatrix} \theta_x \\ \theta_y \end{Bmatrix} + \begin{bmatrix} 1 & 0 \\ 0 & 1 \end{bmatrix} \begin{Bmatrix} \kappa_x \\ \kappa_y \end{Bmatrix}$$

The different FG-CNTMEE material properties can be estimated using the mixture rule as follows [23]:

$$[C] = V_{\text{CNT}} [C^{\text{CNT}}] + V_m [C^m] \quad [e] = V_{\text{CNT}} [e^{\text{CNT}}] + V_m [e^m] \quad [q] = V_{\text{CNT}} [q^{\text{CNT}}] + V_m [q^m] \quad [m] = V_{\text{CNT}} [m^{\text{CNT}}] + V_m [m^m] \quad [\eta] = V_{\text{CNT}} [\eta^{\text{CNT}}] + V_m [\eta^m] \quad [\mu] = V_{\text{CNT}} [\mu^{\text{CNT}}] + V_m [\mu^m] \quad \rho = V_{\text{CNT}} \rho^{\text{CNT}} + V_m \rho^m \quad (3)$$

The various matrices appearing in Eq. (2) can be subdivided based on bending and shear material constants for the sake of simplicity [25].

$$[C_b] = \begin{bmatrix} \widetilde{C}_{11} & \widetilde{C}_{12} & 0 \\ \widetilde{C}_{12} & \widetilde{C}_{22} & 0 \\ 0 & 0 & \widetilde{C}_{66} \end{bmatrix}; [C_s] = \begin{bmatrix} \widetilde{C}_{44} & 0 \\ 0 & \widetilde{C}_{55} \end{bmatrix}; [\mu] = \begin{bmatrix} \widetilde{\mu}_{11} & 0 & 0 \\ 0 & \widetilde{\mu}_{22} & 0 \\ 0 & 0 & \widetilde{\mu}_{33} \end{bmatrix}$$

$$[e_b] = \begin{bmatrix} 0 & 0 & \widetilde{e}_{31} \\ 0 & 0 & \widetilde{e}_{32} \\ 0 & 0 & 0 \end{bmatrix}^T; [e_s] = \begin{bmatrix} 0 & \widetilde{e}_{24} & 0 \\ \widetilde{e}_{15} & 0 & 0 \end{bmatrix}^T; [q_b] = \begin{bmatrix} 0 & 0 & \widetilde{q}_{31} \\ 0 & 0 & \widetilde{q}_{32} \\ 0 & 0 & 0 \end{bmatrix}^T;$$

$$[q_s] = \begin{bmatrix} 0 & \widetilde{q}_{24} & 0 \\ \widetilde{q}_{15} & 0 & 0 \end{bmatrix}^T; [m] = \begin{bmatrix} \widetilde{m}_{11} & 0 & 0 \\ 0 & \widetilde{m}_{22} & 0 \\ 0 & 0 & \widetilde{m}_{33} \end{bmatrix}; [\eta] = \begin{bmatrix} \widetilde{\eta}_{11} & 0 & 0 \\ 0 & \widetilde{\eta}_{22} & 0 \\ 0 & 0 & \widetilde{\eta}_{33} \end{bmatrix} \quad (4)$$

3. Higher order shear deformation theory

The kinematic model of the FG-CNTMEE plate is assumed to follow higher-order shear deformation theory (HSDT) according to which the displacement fields can be represented as:

$$u = u_0 + z\theta_x - \frac{4}{3h^2} z^3 \left(\theta_x + \frac{\partial w_0}{\partial x} \right); \quad v = v_0 + z\theta_y - \frac{4}{3h^2} z^3 \left(\theta_y + \frac{\partial w_0}{\partial y} \right) \quad w = w_0 \quad (5)$$

where, u_0, v_0 , and w_0 are the mid-plane displacements along the x, y , and z -axes, respectively at $z = 0$. The slopes of xz plane and yz plane are denoted by θ_x and θ_y , respectively. The bending strains $\{\varepsilon_b\}$ and shear strains $\{\varepsilon_s\}$ can be shown as:

where $\kappa_x = \frac{\partial \theta_x}{\partial x}, \kappa_y = \frac{\partial \theta_y}{\partial y}$.

4. Finite element formulation

The FE model is developed through eight noded isoparametric element. The degrees of freedom (DOFs) associated with each node are bifurcated into displacement quantities translational $\{d_t^e\}$, rotational $\{d_r^e\}$, higher order rotational $\{d_{r^*}^e\}$, electric potential φ and magnetic potential ψ . The DOFs corresponding to the i th node can be expressed through shape function matrices as follows:

$$\{d_t\} = [N_t] \{d_t^e\}; \{d_r\} = [N_r] \{d_r^e\}; \{d_{r^*}\} = [N_{r^*}] \{d_{r^*}^e\}; \varphi = [N_\varphi] \{\varphi^e\}; \psi = [N_\psi] \{\psi^e\} \quad (7)$$

in which

$$\{d_t^e\} = [u_i \ v_i \ w_i]^T, \quad \{d_r^e\} = [\theta_{xi} \ \theta_{yi}]^T, \quad \{d_{r^*}^e\} = [\kappa_{xi} \ \kappa_{yi}]^T \tag{8}$$

Also, $[N_t]$, $[N_r]$, $[N_{r^*}]$, $[N_\varphi]$ and $[N_\psi]$ are the shape function matrices associated with the degrees of freedom $\{d_t^e\}$, $\{d_r^e\}$, $\{d_{r^*}^e\}$, φ and ψ , respectively which can be expressed as follows:

$$[N_t] = \begin{bmatrix} N_1 & 0 & 0 & N_2 & 0 & 0 & N_8 & 0 & 0 \\ 0 & N_1 & 0 & 0 & N_2 & 0 & \dots & 0 & N_8 & 0 \\ 0 & 0 & N_1 & 0 & 0 & N_2 & 0 & 0 & 0 & N_8 \end{bmatrix} \tag{9}$$

$$[N_r] = [N_{r^*}] = \begin{bmatrix} N_1 & 0 & N_2 & 0 & \dots & N_8 & 0 \\ 0 & N_1 & 0 & N_2 & \dots & 0 & N_8 \end{bmatrix}$$

$$[N_\varphi] = [N_\psi] = [N_1 \ N_2 \ \dots \ N_8]$$

Through the FE parameters mentioned in Eq. (7) – Eq. (9), the strains represented in Eq. (6) can be expressed as

$$\begin{aligned} \{\varepsilon_b\} &= [B_{tb}]\{d_t^e\} + z[B_{rb}]\{d_r^e\} + c_1 z^3 [B_{rb}]\{d_r^e\} \\ &+ c_1 z^3 [B_{rb}]\{d_{r^*}^e\} \quad \{\varepsilon_s\} = [B_{ts}]\{d_t^e\} + [B_{rs}]\{d_r^e\} \\ &+ c_2 z^2 [B_{rs}]\{d_r^e\} + c_2 z^2 [B_{rs}]\{d_{r^*}^e\} \end{aligned} \tag{10}$$

where, $c_1 = -\frac{4}{3h^2}$ and $c_2 = -\frac{4}{h^2}$.

$$\{E\} = [B_\varphi]\{\varphi^e\}; \quad \{H\} = [B_\psi]\{\psi^e\} \tag{11}$$

5. Equation of motion

The Hamilton's principle as adopted for FG-CNTMEE plate can be expressed as follows [22]:

$$\begin{aligned} \delta T_p &= \frac{1}{2} \int_\Omega \delta\{\varepsilon_b\}^T \{\sigma_b\} d\Omega + \frac{1}{2} \int_\Omega \delta\{\varepsilon_s\}^T \{\sigma_s\} d\Omega \\ &- \frac{1}{2} \int_\Omega \delta\{E\}^T \{D\} d\Omega - \frac{1}{2} \int_\Omega \delta\{H\}^T \{B\} d\Omega \\ \delta T_k &= \int_\Omega \delta\{d_t\} \rho \{\ddot{d}_t\} d\Omega \\ \delta T_p + \delta T_k &= 0 \end{aligned} \tag{12}$$

where, T_p , T_k are the potential and kinetic energies, respectively. Further, Ω denotes the volume of the plate. On making use of Eq. (2) – Eq. (11), Eq. (12) can be re-written as follows:

$$\begin{aligned} &= \frac{1}{2} \delta \int_\Omega \left(\{d_{r^*}^e\}^T [B_{rb}]^T c_1 z^3 + \{d_r^e\}^T [B_{rb}]^T c_1 z^3 + \{d_r^e\}^T [B_{rb}]^T z + \{d_t^e\}^T [B_{tb}]^T \right) * \left([C_b][B_{tb}]\{d_t^e\} + z[C_b][B_{rb}]\{d_r^e\} + c_1 z^3 [C_b][B_{rb}]\{d_r^e\} \right. \\ &\quad \left. + c_1 z^3 [C_b][B_{rb}]\{d_{r^*}^e\} \right) \\ &- \{e\}[E] - \{q\}[H] \} \Omega \\ &+ \frac{1}{2} \delta \int_\Omega \left(\{d_{r^*}^e\}^T [B_{rs}]^T c_2 z^2 + \{d_r^e\}^T [B_{rs}]^T c_2 z^2 + \{d_r^e\}^T [B_{rs}]^T + \{d_t^e\}^T [B_{ts}]^T \right) * \left([C_s][B_{ts}]\{d_t^e\} + z[C_s][B_{rs}]\{d_r^e\} + c_2 z^2 [C_s][B_{rs}]\{d_r^e\} \right. \\ &\quad \left. + c_2 z^2 [C_s][B_{rs}]\{d_{r^*}^e\} \right) \\ &- \{e\}[E] - \{q\}[H] \} \Omega \\ &- \frac{1}{2} \delta \int_\Omega \left[\{\varphi\}^T [B_\varphi]^T [e_b]^T [B_{tb}]\{d_t^e\} + \{\varphi\}^T [B_\varphi]^T [e_b]^T z [B_{rb}]\{d_r^e\} + \{\varphi\}^T [B_\varphi]^T [e_b]^T c_1 z^3 [B_{rb}]\{d_r^e\} + \Omega \{\varphi\}^T [B_\varphi]^T [e_s]^T c_2 z^2 [B_{rs}]\{d_r^e\} \right. \\ &\quad \left. + \{\varphi\}^T [B_\varphi]^T [e_b]^T c_1 z^3 [B_{rb}]\{d_{r^*}^e\} + \{\varphi\}^T [B_\varphi]^T [e_s]^T [B_{ts}]\{d_t^e\} + \{\varphi\}^T [B_\varphi]^T [e_s]^T [B_{rs}]\{d_r^e\} + \right. \\ &\quad \left. + \{\varphi\}^T [B_\varphi]^T [e_s]^T c_2 z^2 [B_{rs}]\{d_{r^*}^e\} + \{\varphi\}^T [B_\varphi]^T [\eta][B_\varphi]\{\varphi\} + \{\varphi\}^T [B_\varphi]^T [m][B_\psi]\{\psi\} \right] \Omega \\ &- \frac{1}{2} \delta \int_\Omega \left[\{\psi\}^T [B_\psi]^T [q_b]^T [B_{tb}]\{d_t^e\} + \{\psi\}^T [B_\psi]^T [q_b]^T z [B_{rb}]\{d_r^e\} + \{\psi\}^T [B_\psi]^T [q_b]^T c_1 z^3 [B_{rb}]\{d_r^e\} + \Omega \right. \\ &\quad \left. + \{\psi\}^T [B_\psi]^T [q_b]^T c_1 z^3 [B_{rb}]\{d_{r^*}^e\} + \{\psi\}^T [B_\psi]^T [q_s]^T [B_{ts}]\{d_t^e\} + \{\psi\}^T [B_\psi]^T [q_s]^T [B_{rs}]\{d_r^e\} + \right. \end{aligned} \tag{13}$$

The present study assumes that the free charge and current densities are absent and electromagnetic fields exhibit quasi-static behaviour. Further, using the Maxwell's equations, the electric intensity (E) and the magnetic intensity (H) are related to the electric potential (φ) and magnetic potential (ψ), respectively as [22]:

The coefficients of $\{d_t^e\}$, $\{d_r^e\}$, $\{d_{r^*}^e\}$, φ and ψ are bifurcated and stiffness matrices are assigned (see Appendix). Further, by implementing condensation technique, the equations of motion are obtained, which can be represented as follows [23]:

Table 2
The material properties of CNT fiber and piezoelectric matrix used for CNTMEE plate [23,62].

Material property	Material constants	CNT	PVDF	Barium Titanate
Elastic constants (GPa)	C_{11}	5825	2.815	166
	$C_{12} = C_{21}$	1019	1.081	77
	C_{22}	7304	2.815	166
	$C_{44} = C_{55} = C_{66}$	1945	0.8671	43
Piezoelectric constants ($C \cdot m^{-2}$)	e_{31}	0	-0.13	-4.4
Dielectric constant ($10^{-9} C^2 N^{-1} m^{-2}$)	ϵ_{33}	0	0.106	11.2
Magnetic permeability ($N s^2 \cdot C^{-2}$)	μ_{33}	0.25	$4\pi \times 10^{-7}$	0.05
Piezomagnetic constants ($N \cdot Am^{-1}$)	q_{31}	22	0	0
Magneto-electric constant ($10^{-12} N s \cdot VC^{-1}$)	m_{33}	0	-46	1500
Density($kg \cdot m^{-3}$)	ρ	1400	1780	5800

$$\begin{aligned}
 [M_{tt}^e] \{d_t^e\} + [K_{tt}^e] \{d_t^e\} + [K_{tr}^e] \{d_r^e\} + [K_{tr*}^e] \{d_{r*}^e\} + [K_{t\phi}^e] \varphi^e + [K_{t\psi}^e] \psi^e &= 0 \\
 [K_{tr}^e]^T \{d_t^e\} + [K_{tr}^e] \{d_r^e\} + [K_{tr*}^e] \{d_{r*}^e\} + [K_{r\phi}^e] \varphi^e + [K_{r\psi}^e] \psi^e &= 0 \\
 [K_{tr*}^e]^T \{d_t^e\} + [K_{tr*}^e] \{d_r^e\} + [K_{tr**}^e] \{d_{r*}^e\} + [K_{r*\phi}^e] \varphi^e + [K_{r*\psi}^e] \psi^e &= 0 \\
 [K_{t\phi}^e]^T \{d_t^e\} + [K_{t\phi}^e] \{d_r^e\} + [K_{t*\phi}^e] \{d_{r*}^e\} - [K_{\phi\phi}^e] \varphi^e - [K_{\phi\psi}^e] \psi^e &= 0 \\
 [K_{t\psi}^e]^T \{d_t^e\} + [K_{t\psi}^e] \{d_r^e\} + [K_{t*\psi}^e] \{d_{r*}^e\} - [K_{\psi\phi}^e] \varphi^e - [K_{\psi\psi}^e] \psi^e &= 0
 \end{aligned}
 \tag{14}$$

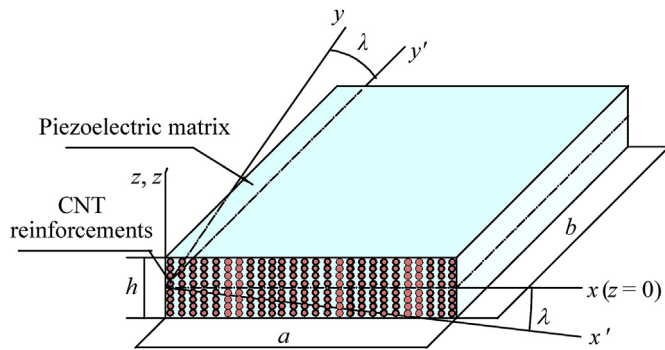


Fig. 1. Schematic representation of FG-CNTMEE plate.

The transformation of Eq. (14) to accommodate skew angle variations is illustrated in Appendix.

6. Problem statement

In this study, the frequency characteristics of FG-CNTMEE plates are evaluated through FE formulation. The material properties of FG-CNTMEE depicted in Table 2 are considered in this work. Ac-

Table 3
Convergence of the natural frequency of MEE plate with mesh size.

Mode No.	Mesh size				Moita et al. [66]
	4 × 4	6 × 6	8 × 8	10 × 10	
1	2422.14	2428.60	2432.14	2432.21	2449.7
2	6255.74	6264.67	6268.31	6268.40	6280.6
3	6255.74	6264.67	6268.31	6268.40	6280.6

the plate and x' , y' - and z' - axes are the transformation axes. In this study, $a = b = 0.1$ m; $h = 0.03$ m are considered for evaluation. The various CNT distribution patterns and its mathematical expressions are shown in Table 1. Further, the open and closed electro-magnetic boundary conditions are enforced on the FG-CNTMEE plates, which can be represented as follows:

$$\begin{aligned}
 \text{Closed – circuit: } \varphi = \psi = 0 \quad \left(z = \pm \frac{h}{2} \right) \quad \text{Open – circuit: } D_z \\
 = B_z = 0 \quad \left(z = \pm \frac{h}{2} \right)
 \end{aligned}
 \tag{15}$$

Analogously, the mechanical boundary constraints employed in this work can be explicitly represented as

$$\begin{aligned}
 \text{Clamped edge (C): } u = v = w = \theta_x = \theta_y = \kappa_x = \kappa_y = \varphi = \psi = 0 \quad \text{Simply supported edge (S):} \\
 u = \theta_x = \kappa_x \neq 0; v = w = \varphi = \psi = 0 \text{ at } x = 0, av = \theta_y = \kappa_y \neq 0; u = w = \varphi = \psi = 0 \text{ at } y = 0, b
 \end{aligned}
 \tag{16}$$

According to Fig. 1(a), a , b and h represents the length, width and thickness of the FG-CNTMEE plate. Further, λ is the skew angle of

Table 4
Convergence and comparison of the fundamental frequency of MEE plates ($a = b = 1$ m; $h = 0.3$ m; $\lambda = 15^\circ$).

Mesh	Computation Time/s	No. DOF	No. Elements	Frequency ($\times 10^4$ rad s^{-1})
Present FE model				
4 \times 4	0.87	455	16	1.345
6 \times 6	1.05	931	36	1.363
8 \times 8	2.06	1575	64	1.381
10 \times 10	5.25	2387	100	1.384
COMSOL solutions				
Coarser	5.56	4604	478	1.046
Coarse	7.82	8212	874	1.187
Normal	12.34	15,209	1665	1.295
Fine	20.76	36,086	4293	1.368
Finer	57.81	87,147	10,810	1.370

Table 5
Validation of the FE formulation for skew MEE plates (BFB stacking sequence, SSSS boundary condition).

Mode No.	Skew Angles					
	$\lambda = 15^\circ$		$\lambda = 30^\circ$		$\lambda = 45^\circ$	
	Kiran and Kattimani [67]	Present	Kiran and Kattimani [67]	Present	Kiran and Kattimani [67]	Present
1	13270.48	13271.3	15615.46	15616.7	20720.13	20721.2
2	24725.53	24726.7	26519.32	26520.6	31404.56	31405.6
3	27428.19	27430.1	32607.70	32608.7	41411.75	41412.8

7. Results and discussion

In this section the coupled structural response of FG-CNTMEE plates subjected to various electromagnetic (EM) boundary conditions are studied via FE formulation depicted in earlier section. Initially, to verify the credibility of the proposed formulation to incorporate coupling fields, geometrical skewness and FG-CNTs, the results of present study are compared with previously published literature [15,66,67]. The convergence study depicted in Table 3 and Table 4 suggest that for a mesh size of 10×10 the results converge with that of Moita et al. [66]. In addition, the verification results illustrated in Table 5 –and 6 affirm that there exist a good correlation between the results and hence the proposed FE formulation is efficient enough to accommodate geometrical skewness and FG-CNTs. Therefore, it is justified that the proposed formulation can be extended to examine the influence of EM boundary conditions on the frequencies of FG-CNTMEE plate. Also, parametric study has been performed to assess the

effect of CNT distributions, volume fraction, skew angle, aspect ratio, length-to-thickness ratio and coupling fields on frequency response of FG-CNTMEE plates with different EM conditions.

7.1. Effect of open and closed circuit conditions

The variation in the first three natural frequencies of FG-CNTMEE plate with UD distribution and $V_{\text{CNT}}^* = 0.12$ subjected to different EM conditions is shown in Table 7. Two variants of FG-CNTMEE plates with all sides clamped (CCCC) and all sides simply supported (SSSS) are considered for evaluation. It was found that for both the cases of constraints a better frequency response was observed for open circuit EM condition in contrast to the closed circuit EM condition. This may be attributed to the fact that open circuit EM condition exhibit an enhanced energy release capability which adds up to the stiffness of the plate. Also, it is worth noticing that the EM conditions have a pronounced effect on the higher modes.

7.2. Effect of piezoelectric matrix material

Table 8 encapsulates the effect of piezoelectric matrix materials viz. PVDF and BaTiO₃ on the fundamental natural frequency of FG-CNTMEE plate. As seen from the table, a predominant influence of PVDF over BaTiO₃ is noticed due to higher piezoelectric coefficients. In addition, the significant influence of EM condition prevails on the FG-CNTMEE plate with PVDF as the matrix as opposed to BaTiO₃

Table 6
Validation for skew FG-CNT plates ($\lambda = 30^\circ$; $V_{\text{CNT}}^* = 0.12$; CCCC boundary condition).

CNT Pattern	1st Mode		2nd Mode		3rd Mode	
	Kiani [15]	Present	Kiani [15]	Present	Kiani [15]	Present
UD	9.0583	9.064	11.7968	11.823	16.8446	16.856
FG-X	9.6602	9.6711	12.4074	12.476	17.5573	17.579
FG-O	7.9610	7.9670	10.8772	10.883	15.9129	15.934
FG-V	8.4951	8.4968	11.4120	11.441	16.5463	16.643

Table 7
Effect of electromagnetic boundary conditions on first three natural frequencies ($\times 10^3$ rad s^{-1}) of CNTMEE plate.

Mode No.	CCCC			SSSS		
	Open circuit	Closed circuit	% difference	Open circuit	Closed circuit	% difference
1	38.9	38.2	1.77	32.6	32.1	1.45
2	42.1	41.3	1.96	36.2	35.6	1.58
3	53.5	52.2	2.43	44.2	43.4	1.89

% difference = [(Open circuit-closed circuit)/closed circuit] \times 100.

Table 8
Effect of electromagnetic boundary conditions and piezoelectric matrix material on fundamental natural frequency ($\times 10^3 \text{ rad}\cdot\text{s}^{-1}$) of CNTMEE plate (SSSS).

CNT distribution	CNT + PVDF			CNT + BaTiO ₃		
	Open circuit	Closed circuit	% difference	Open circuit	Closed circuit	% difference
	$V^*_{\text{CNT}} = 0.12$					
FG-X	47.5	46.6	1.93	28.8	28.4	1.24
UD	38.7	38.2	1.25	24.3	24.1	0.81
FG-O	27.4	27.3	0.39	18.74	18.7	0.25
FG-V	31.7	31.4	0.96	21.53	21.4	0.62
	$V^*_{\text{CNT}} = 0.17$					
FG-X	57.4	55.8	2.87	34.56	33.8	2.27
UD	46.6	45.7	1.86	28.81	28.4	1.47
FG-O	32.8	32.6	0.58	21.7	21.6	0.46
FG-V	38.03	37.5	1.42	25.1	24.8	1.12
	$V^*_{\text{CNT}} = 0.28$					
FG-X	75.2	72.5	3.67	46.11	44.7	3.16
UD	60.8	59.4	2.38	38.0	37.2	2.05
FG-O	42.6	42.3	0.74	27.9	27.7	0.64
FG-V	49.6	48.7	1.82	32.3	31.8	1.57

% difference = [(Open circuit-closed circuit)/closed circuit] \times 100.

7.3. Effect of CNT distribution and volume fraction

The influence of different CNT distribution patterns and volume fraction on the frequency response of FG-CNTMEE plates with PVDF and BaTiO₃ as matrix is illustrated in Fig. 2(a) - Fig. 2(d). It can be

inferred from the figure that among the various CNT distributions selected, FG-X pattern yields a higher frequency. This may be attributed to the higher flexural stiffness exhibited by FG-X distribution. In addition, a predominant influence of EM conditions can be noticed in the order of FG-X > UD > FG-V > FG-O. Thus, by

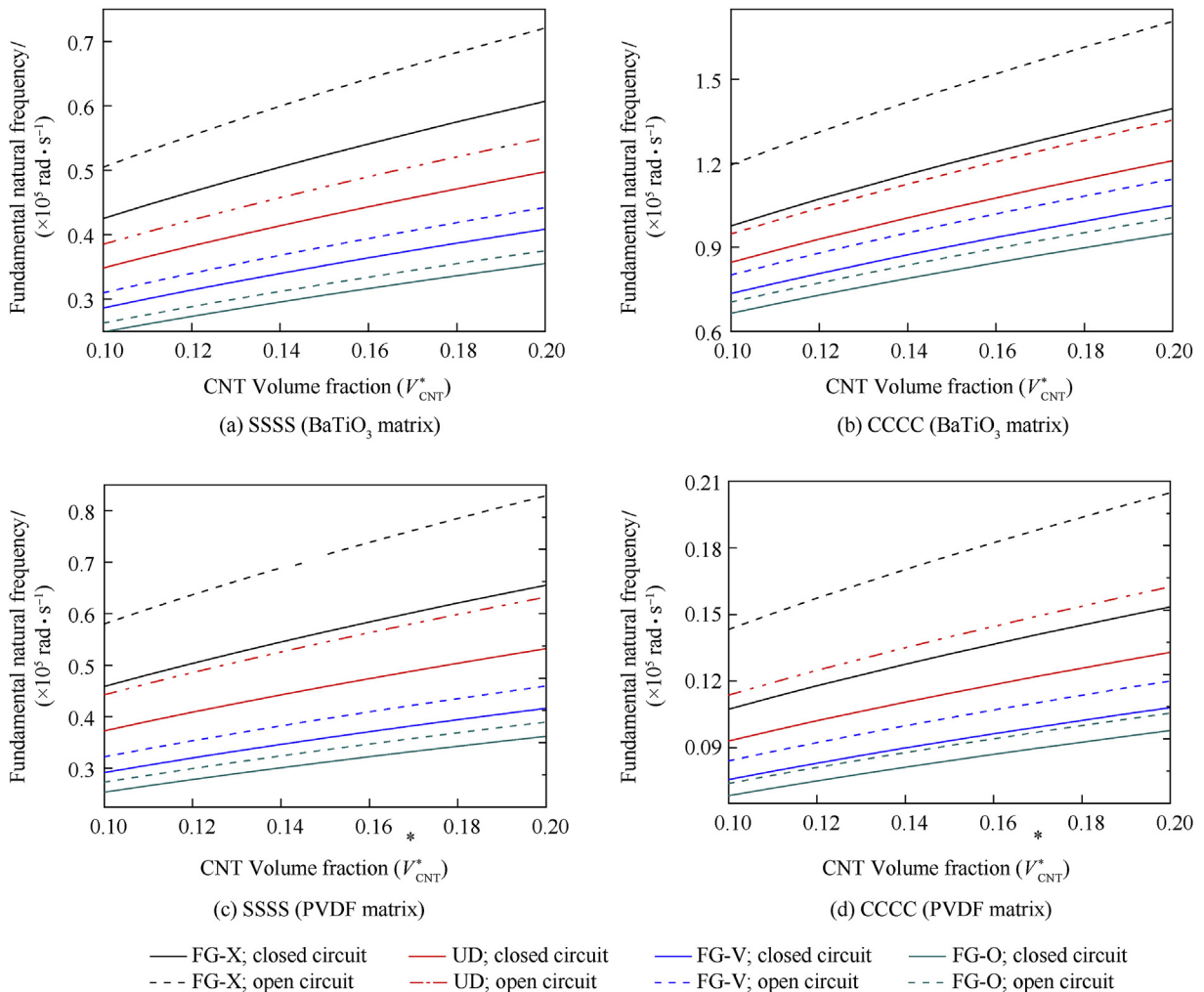


Fig. 2. Effect of volume fraction and CNT distributions on FG-CNTMEE plates.

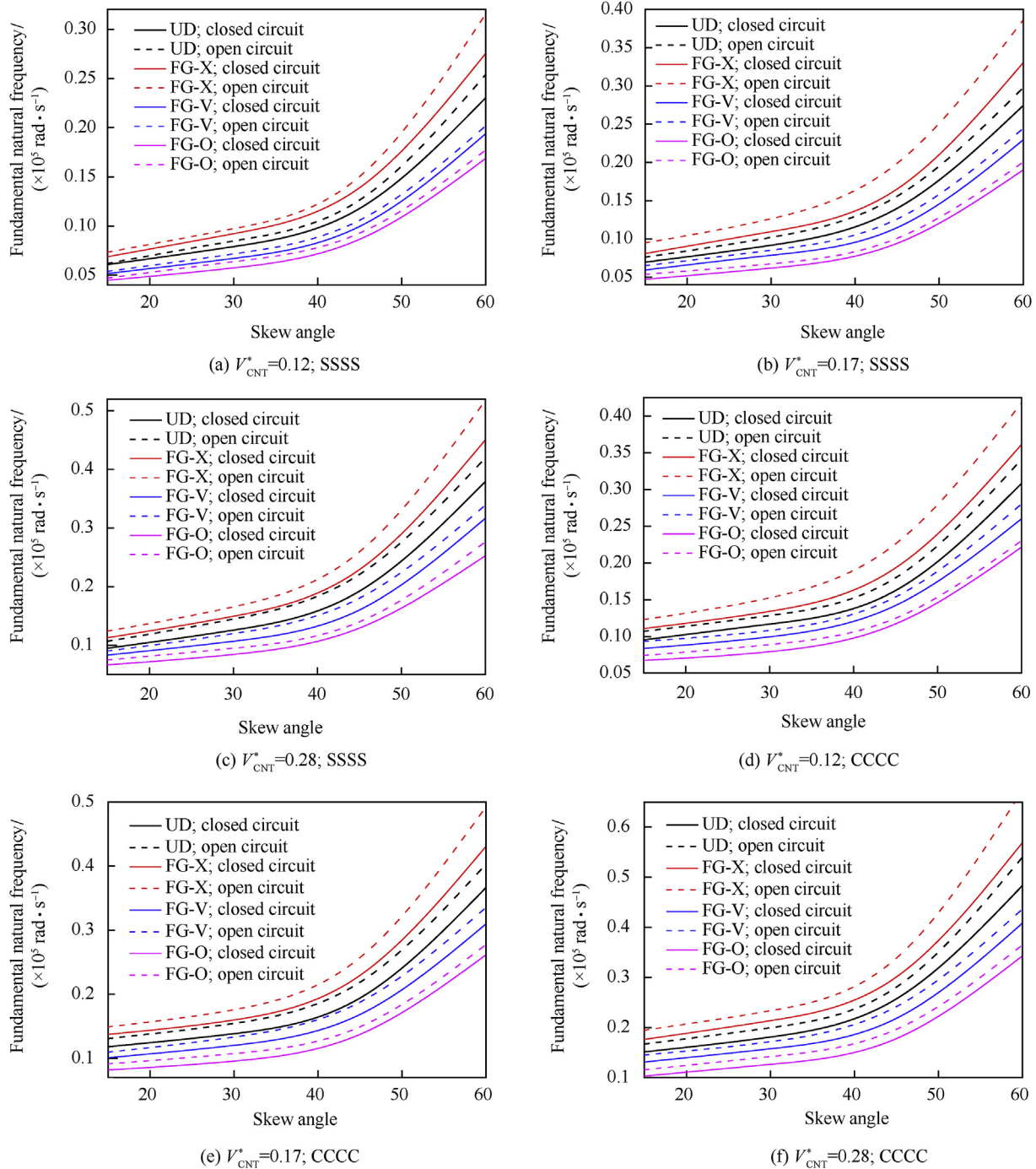


Fig. 3. Effect of skew angle on FG-CNTMEE plates with different CNT volume fractions.

adjusting the distribution of CNTs along the thickness direction, the desired stiffness of the plates can be achieved and noted that reinforcement distributed close to the top and bottom of plates are more efficient than those distributed nearby the mid-plane for increasing the stiffness of plates.

Meanwhile, it is also witnessed that for the CNTs distribution pattern considered, the volume fraction of CNTs has a greater influence on the frequency response. A higher volume fraction of CNTs enhances the frequency of the plate as the stiffness is improved. A minute variation in the volume of CNTs results in drastic increase in the natural frequency. As expected, the results

suggest that the discrepancies between the open circuit and closed circuit natural frequencies improve with higher volume fraction as noticed from Table 8.

7.4. Effect of skew angle (λ)

Fig. 3(a) – Fig. 3(f), illustrate the effect of EM conditions associated with the different skew angles of FG-CNTMEE plates. Based on the results of these figures, it is worth to noticing that with an improvement in the skew angle, the fundamental natural frequency improves. Further, it can also be witnessed that at lower

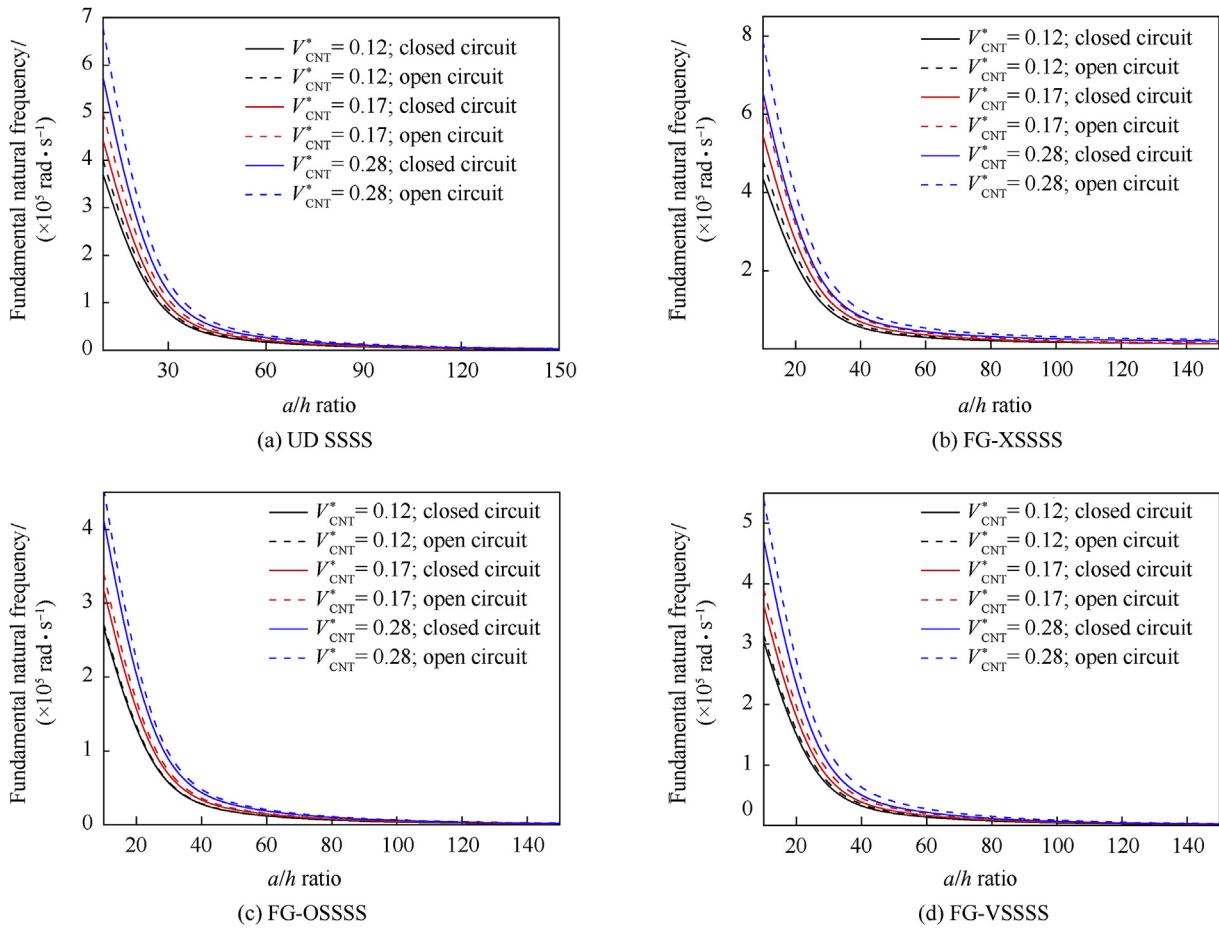


Fig. 4. Effect of a/h ratio associated with EM conditions on the fundamental natural frequency of FG-CNTMEE plates with different CNT volume fractions (SSSS condition).

skew angle, the influence of EM conditions are negligible. However, as the skew angles improve, its effect also becomes proportionally significant. This may be due to the fact that at higher skew angles the stiffness and the energy release capabilities of the plate enhances due to minimum area. In addition, a predominant influence of FG-X distribution it observed here as well.

7.5. Effect of aspect (a/h) ratio

In order to evaluate the effect of a/h ratios in conjunction with EM conditions, numerical analysis has been performed considering FG-CNTMEE plate with various CNT volume fractions and results are highlighted in Fig. 4 and Fig. 5, respectively for SSSS and CCC conditions. It can be seen from these figures that irrespective of the CNT distribution patterns, lower aspect ratio has a pronounced effect on the frequency. This is due to higher degree of coupling displayed by thick FG-CNTMEE plates. In addition, the influence of EM conditions on the frequency diminishes as the plate moves from thick to thin category. In other words, predominant effect of EM conditions is witnessed for FG-CNTMEE plates with less a/h ratios rather than higher a/h ratios.

7.6. Effect of a/b ratio

The results related to frequency of FG-CNTMEE plate with different a/b ratio is summarised in Fig. 6(a) – Fig. 6(d). It can be

clearly seen from these figures that for all the CNT distribution patterns considered, a higher value of a/b ratio results in dramatically reduced frequency values. This may be due to the nearing of beam behaviour with higher a/b ratio. Additionally, the influence of EM conditions are negligible at higher a/b ratio which gradually improves and magnifies at the lower a/b ratio. A similar conclusion drawn with reference to a/h ratio can be witnessed here as well.

7.7. Effect of boundary conditions

The influence of EM circuit conditions with different essential mechanical boundary conditions is evaluated in Table 9. As expected, the significant effect of open circuit conditions over closed circuit improves with more number of clamped edges owing to higher energy release from open circuit condition and higher rigidity of the plate with more number of clamped edges.

7.8. Effect of coupling fields

The coupled natural frequency of FG-CNTMEE plates is the summation of contribution from magnetic, electric and elastic fields. It becomes very much crucial to evaluate the effects of different fields. Tables 10–13 show the influence of coupling fields associated with the EM circuit conditions on the natural frequencies of FG-CNTMEE plate with various skew angles. It can be witnessed from this analysis that as opposed to closed circuit, open

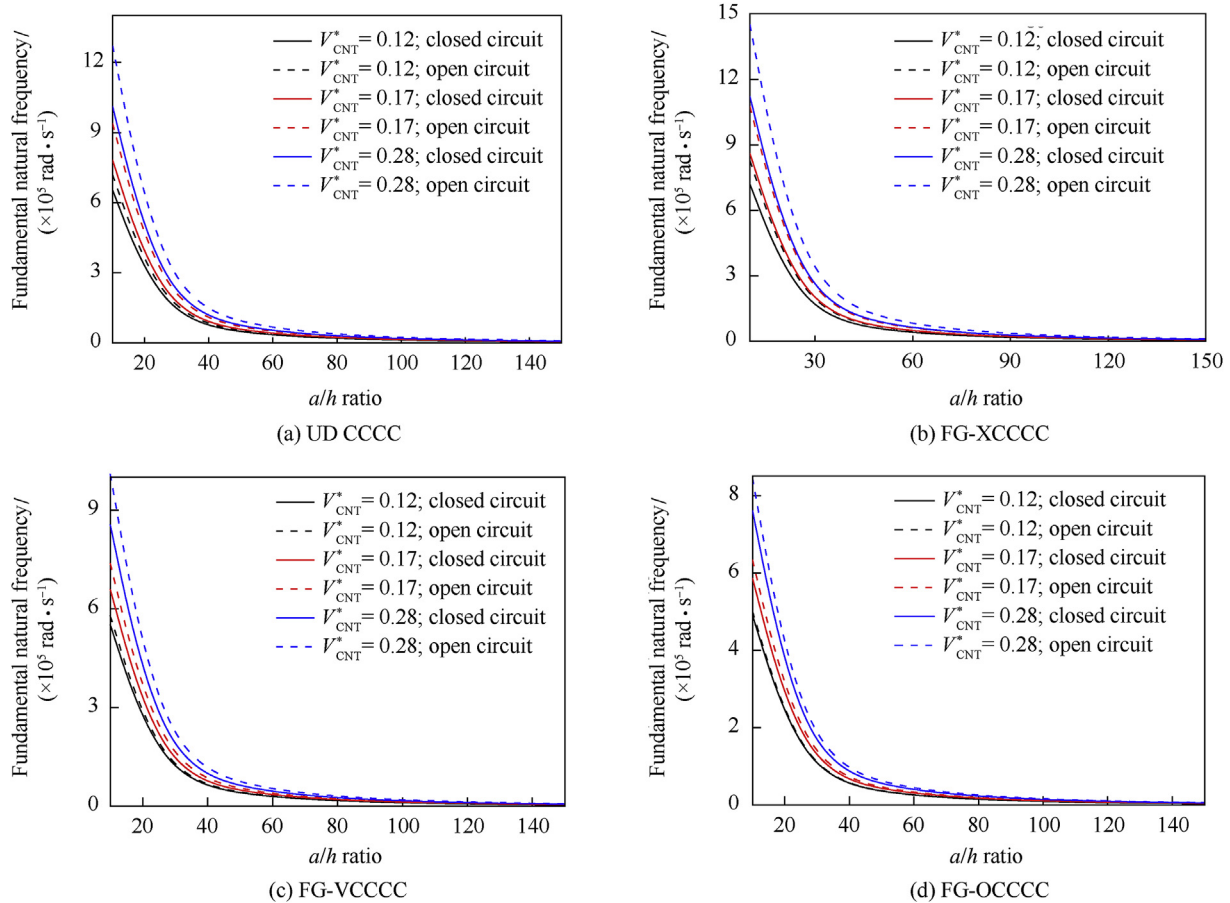


Fig. 5. Effect of a/h ratio associated with EM conditions on the fundamental natural frequency of FG-CNTMEE plates with different CNT volume fractions (CCCC condition).

circuit condition has a predominant effect on the percentage difference between the natural frequencies obtained from complete coupling and elastic field alone. Further, as depicted from Fig. 7(a) and Fig. 7(b), the percentage difference between completely coupled and elastic frequencies magnifies with higher skew angle. Also, FG-CNTMEE plate with FG-X distribution subjected to open circuit condition exhibit a significant effect.

8. Conclusions

In this article, the coupled frequency response of FG-CNTMEE plates has been evaluated considering the effect of open and closed circuit electro-magnetic boundary conditions. To this end, higher order finite element formulation has been developed and equations of motion are arrived via Hamilton's principle. The C^1 continuity requirement of HSDT is fulfilled by considering second order derivative terms as higher order rotational degrees of freedom. Therefore, its computational efficiency is found to be better than the numerical software in terms of computational time and costs.

The following conclusions can be drawn out of the numerical evaluation.

- In contrast to closed circuit condition a beneficial effect of open circuit condition on the natural frequencies is witnessed. The maximum percentage difference open and closed circuit natural

frequencies of CNTMEE plate is about 2.43% and 1.89%, for CCCC and SSSS conditions, respectively

- Alongside, FG-X CNT distribution exhibit more coupling frequency when subjected to open circuit condition, due to higher flexural rigidity offered. For $V_{CNT}^* = 0.28$ and $V_{CNT}^* = 0.12$, the percentage difference between the open and closed circuit fundamental natural frequencies is found to be maximum and minimum with 3.67% and 1.93%, respectively.
- At higher skew angle, CNT volume fraction and length-to-width ratio the discrepancies between open and closed circuit frequencies magnifies. Meanwhile, a reverse trend is noticed for aspect ratio.
- The coupling fields exhibit a higher frequency than elastic field alone and this difference improves with volume fraction of CNT and skew angle. For a higher skew angle of 60° , Open circuit condition yields an improvement in coupled frequency by 3.65%, where as the closed circuit condition results in 3.51% enhancement.

It is believed that the proposed formulation and the results obtained may serve as benchmark solutions for future design and analysis of smart structures. However, the limitation of this formulation is that it does not consider the influence of external environment or loadings on the frequency analysis, which may be a novel research gap for the future evaluation.

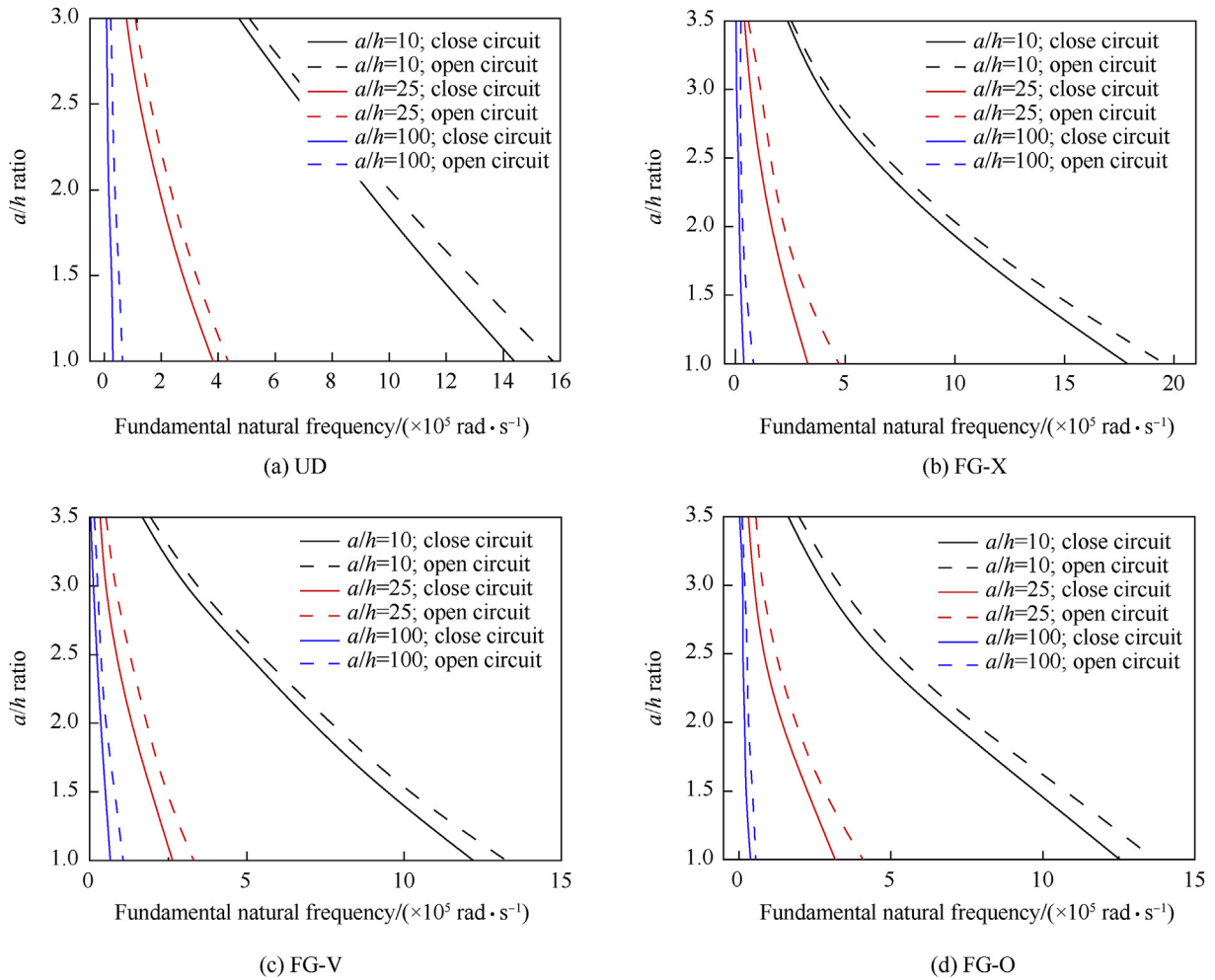


Fig. 6. Effect of a/h ratio associated with EM conditions on the fundamental natural frequency of FG-CNTMEE plates with aspect ratio and CNT distributions.

Table 9

Effect of mechanical boundary conditions on fundamental natural frequency ($\times 10^3 \text{ rad}\cdot\text{s}^{-1}$) of CNTMEE plate with different electromagnetic boundary conditions.

CNT distribution		CCCC	SCSS	SCSC	CFCF	CCFF
UD	Open circuit	95.6	50.01	64.94	44.2	14.4
	Closed circuit	93.2	49.1	63.4	43.5	14.2
	% difference	2.75	1.86	2.43	1.64	1.21
FG-X	Open circuit	110.6	59.63	78.3	54.7	17.53
	Closed circuit	107.3	58.4	76.2	53.7	17.3
	% difference	3.13	2.11	2.76	1.86	1.37
FG-O	Open circuit	80.7	36.82	49.34	32.1	10.18
	Closed circuit	79.3	36.4	48.6	31.8	10.1
	% difference	1.72	1.16	1.52	1.02	0.75
FG-V	Open circuit	82.6	41.05	54.35	36.01	11.42
	Closed circuit	80.6	40.37	53.17	35.49	11.3
	% difference	2.50	1.69	2.21	1.49	1.10

% difference = [(Open circuit-closed circuit)/closed circuit] \times 100.

Table 10

Effect of coupling fields on fundamental natural frequency ($\times 10^3 \text{ rad}\cdot\text{s}^{-1}$) of CNTMEE plate with different electromagnetic boundary conditions and skew angles (FG-X distribution; BaTiO₃ material).

Skew Angle	Open circuit			Closed circuit		
	MEE coupling	Elastic	Difference/%	MEE coupling	Elastic	Difference/%
0	110.3	107.6	2.94	107.2	104.2	2.75
15	121.5	117.8	3.06	112.8	109.6	2.86
30	138.4	133.9	3.25	120.4	116.7	3.04
45	156.8	151.3	3.54	132.2	127.8	3.31
60	170.2	163.4	4.03	147.3	141.8	3.77

Difference (%) = (MEE coupling- Elastic)/MEE coupling.

Table 11

Effect of coupling fields on fundamental natural frequency ($\times 10^3 \text{ rad}\cdot\text{s}^{-1}$) of CNTMEE plate with different electromagnetic boundary conditions and skew angles (UD distribution; BaTiO₃ material).

Skew Angle	Open circuit			Closed circuit		
	MEE coupling	Elastic	Difference/%	MEE coupling	Elastic	Difference/%
0	95.8	93.25	2.66	92.9	90.52	2.56
15	103.4	100.53	2.77	98.3	95.68	2.66
30	111.6	108.32	2.94	107.3	104.24	2.83
45	128.5	123.59	3.20	121.5	117.76	3.08
60	148.7	143.3	3.65	137.2	132.38	3.51

Difference (%) = (MEE coupling- Elastic)/MEE coupling.

Table 12

Effect of coupling fields on fundamental natural frequency ($\times 10^3 \text{ rad}\cdot\text{s}^{-1}$) of CNTMEE plate with different electromagnetic boundary conditions and skew angles (FG-V distribution; BaTiO₃ material).

Skew Angle	Open circuit			Closed circuit		
	MEE coupling	Elastic	Difference/%	MEE coupling	Elastic	Difference/%
0	83.2	81.19	2.41	80.6	78.69	2.37
15	88.7	86.47	2.51	83.4	81.35	2.46
30	101.2	98.5	2.67	94.7	92.22	2.61
45	115.9	112.54	2.90	105.6	102.6	2.85
60	133.4	128.98	3.31	120.3	116.40	3.24

Difference (%) = (MEE coupling- Elastic)/MEE coupling.

Table 13

Effect of coupling fields on fundamental natural frequency ($\times 10^3 \text{ rad}\cdot\text{s}^{-1}$) of CNTMEE plate with different electromagnetic boundary conditions and skew angles (FG-O distribution; BaTiO₃ material).

Skew Angle	Open circuit			Closed circuit		
	MEE coupling	Elastic	Difference/%	MEE coupling	Elastic	Difference/%
0	74.1	72.46	2.21	72.9	71.33	2.15
15	79.2	77.47	2.32	74.5	72.83	2.23
30	89.4	87.22	2.43	83.5	81.52	2.37
45	103.6	100.88	2.62	95.8	93.32	2.58
60	120.6	117.0	2.99	110.3	107.10	2.94

Difference (%) = (MEE coupling- Elastic)/MEE coupling.

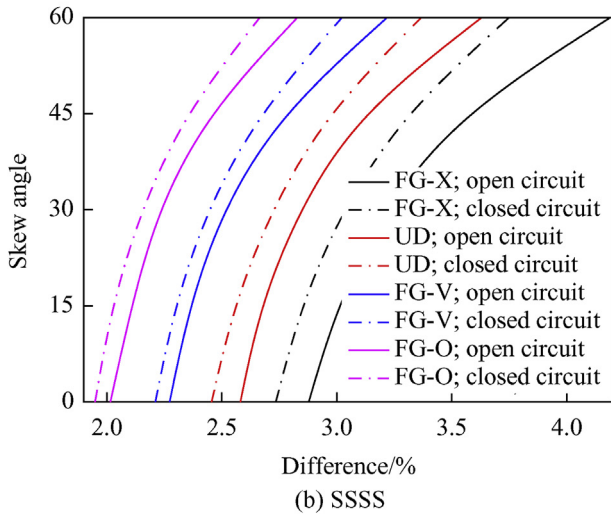
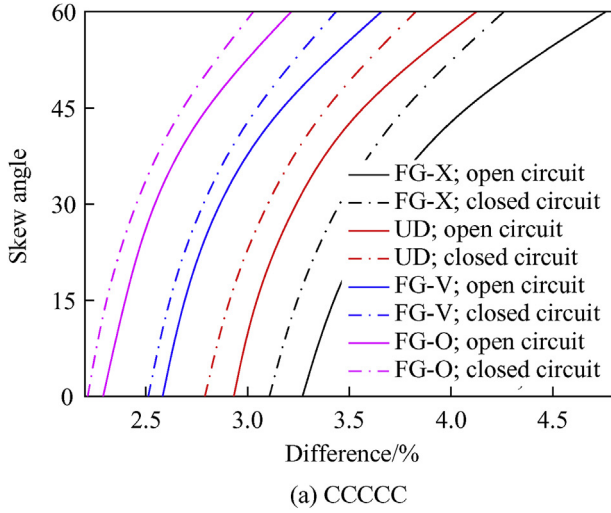


Fig. 7. Effect of skew angles, EM conditions and FG-CNT distributions on %difference in fundamental natural frequency of FG-CNTMEE plate with different coupling fields (PVDF piezoelectric matrix).

Acknowledgements

The first author acknowledges the support of Indian Institute of Science, Bangalore, through C.V. Raman Post-doctoral fellowship, under Institution of Eminence scheme.

Appendix

The derivative of shape function matrices appearing in Eq. (10) can be represented by

$$[B_{tb}] = \begin{bmatrix} N_{i,x} & 0 & 0 \\ 0 & N_{i,y} & 0 \\ N_{i,y} & N_{i,x} & 0 \end{bmatrix}, [B_{rb}] = \begin{bmatrix} N_{i,x} & 0 \\ 0 & N_{i,y} \\ N_{i,y} & N_{i,x} \end{bmatrix}, \tag{A-1}$$

$$[B_{ts}] = \begin{bmatrix} 0 & 0 & N_{i,x} \\ 0 & 0 & N_{i,y} \end{bmatrix}, [B_{rs}] = \begin{bmatrix} 1 & 0 \\ 0 & 1 \end{bmatrix}$$

The explicit representation of the stiffness matrices appearing in Eq. (14) can be shown as follows:

$$[K_{tt}^e] = [K_{tb1}^e] + [K_{ts1}^e], [K_{tr}^e] = [K_{rtb24}^e]^T + [K_{rts13}^e]^T [K_{tr}^*] = [K_{rtb4}^e]^T + [K_{rts3}^e]^T, [K_{t\varphi}^e] = [K_{tb\varphi1}^e] + [K_{ts\varphi1}^e],$$

$$[K_{t\psi}^e] = [K_{tb\psi1}^e] + [K_{t\psi s1}^e], [K_{rr}^e] = [K_{rbb5735}^e] + [K_{rrs3513}^e], [K_{rr}^*] = [K_{rbb57}^e] + [K_{rrs35}^e], [K_{r\varphi}^e] = [K_{rb\varphi24}^e] + [K_{r\varphi s13}^e],$$

$$[K_{r\psi}^e] = [K_{rb\psi24}^e] + [K_{r\psi s13}^e], [K_{r^*r^*}^e] = [K_{rbb7}^e] + [K_{rrs5}^e], [K_{r^*\varphi}^e] = [K_{rb\varphi4}^e] + [K_{r\varphi s3}^e],$$

$$[K_{r^*\psi}^e] = [K_{rb\psi4}^e] + [K_{r\psi s3}^e] [K_{rtt}^e] = [K_{rtb24}^e] + [K_{rts13}^e], \tag{A-2}$$

$$[K_{rbb5735}^e] = [K_{rbb57}^e] + [K_{rbb35}^e], [K_{rrs3513}^e] = [K_{rrs35}^e] + [K_{rrs13}^e],$$

$$[K_{rbb57}^e] = [K_{rbb5}^e] + [K_{rbb7}^e], [K_{rbb35}^e] = [K_{rbb3}^e] + [K_{rbb5}^e], [K_{rrs35}^e] = [K_{rrs3}^e] + [K_{rrs5}^e], [K_{rrs13}^e] = [K_{rrs1}^e] + [K_{rrs3}^e],$$

$$[K_{rb\varphi24}^e] = [K_{rb\varphi2}^e] + [K_{rb\varphi4}^e], [K_{r\varphi s13}^e] = [K_{r\varphi s1}^e] + [K_{r\varphi s3}^e],$$

$$[K_{rb\psi24}^e] = [K_{rb\psi2}^e] + [K_{rb\psi4}^e], [K_{r\psi s13}^e] = [K_{r\psi s1}^e] + [K_{r\psi s3}^e]$$

where,

$$\begin{aligned}
 [K_{\psi\psi}^e] &= \int_0^a \int_0^b [B_\psi]^T [D_{\psi\psi}] [B_\psi] \, dx \, dy, [K_{\varphi\varphi}^e] = \int_0^a \int_0^b [B_\varphi]^T [D_{\varphi\varphi}] [B_\varphi] \, dx \, dy, \\
 [K_{tb1}^e] &= \int_0^a \int_0^b [B_{tb}]^T [D_{b1}] [B_{tb}] \, dx \, dy, [K_{ts1}^e] = \int_0^a \int_0^b [B_{ts}]^T [D_{s1}] [B_{ts}] \, dx \, dy, [K_{rtb4}^e] = \int_0^a \int_0^b [B_{rb}]^T [D_{b4}] [B_{rb}] \, dx \, dy, \\
 [K_{rts3}^e] &= \int_0^a \int_0^b [B_{rs}]^T [D_{s3}] [B_{ts}] \, dx \, dy, [K_{t\psi1}^e] = \int_0^a \int_0^b [B_{tb}]^T [D_{b\psi1}] [B_\psi] \, dx \, dy, [K_{ts\varphi1}^e] = \int_0^a \int_0^b [B_{ts}]^T [D_{s\varphi1}] [B_\varphi] \, dx \, dy \\
 [K_{tb\psi1}^e] &= \int_0^a \int_0^b [B_{tb}]^T [D_{b\psi1}] [B_\psi] \, dx \, dy, [K_{ts\psi1}^e] = \int_0^a \int_0^b [B_{ts}]^T [D_{s\psi1}] [B_\psi] \, dx \, dy, \\
 [K_{rrb7}^e] &= \int_0^a \int_0^b [B_{rb}]^T [D_{b7}] [B_{rb}] \, dx \, dy, [K_{rrs5}^e] = \int_0^a \int_0^b [B_{rs}]^T [D_{s5}] [B_{rs}] \, dx \, dy, [K_{rb\varphi4}^e] = \int_0^a \int_0^b [B_{rb}]^T [D_{b\varphi4}] [B_\varphi] \, dx \, dy \\
 [K_{r\varphi s3}^e] &= \int_0^a \int_0^b [B_{rs}]^T [D_{s\varphi3}] [B_\varphi] \, dx \, dy, \\
 [K_{rb\psi4}^e] &= \int_0^a \int_0^b [B_{rb}]^T [D_{b\psi4}] [B_\psi] \, dx \, dy, [K_{r\psi s3}^e] = \int_0^a \int_0^b [B_{rs}]^T [D_{s\psi3}] [B_\psi] \, dx \, dy, \\
 [K_{rrb5}^e] &= \int_0^a \int_0^b [B_{rb}]^T [D_{b5}] [B_{rb}] \, dx \, dy, [K_{rrb7}^e] = \int_0^a \int_0^b [B_{rb}]^T [D_{b7}] [B_{rb}] \, dx \, dy, [K_{rrb3}^e] = \int_0^a \int_0^b [B_{rb}]^T [D_{b3}] [B_{rb}] \, dx \, dy, \\
 [K_{rrs1}^e] &= \int_0^a \int_0^b [B_{rs}]^T [D_{s1}] [B_{rs}] \, dx \, dy, [K_{rrs3}^e] = \int_0^a \int_0^b [B_{rs}]^T [D_{s3}] [B_{rs}] \, dx \, dy, [K_{rrs5}^e] = \int_0^a \int_0^b [B_{rs}]^T [D_{s5}] [B_{rs}] \, dx \, dy, \\
 [K_{rb\varphi2}^e] &= \int_0^a \int_0^b [B_{rb}]^T [D_{b\varphi2}] [B_\varphi] \, dx \, dy, [K_{rb\varphi4}^e] = \int_0^a \int_0^b [B_{rb}]^T [D_{b\varphi4}] [B_\varphi] \, dx \, dy \\
 [K_{rb\psi2}^e] &= \int_0^a \int_0^b [B_{rb}]^T [D_{b\psi2}] [B_\psi] \, dx \, dy, [K_{rb\psi4}^e] = \int_0^a \int_0^b [B_{rb}]^T [D_{b\psi4}] [B_\psi] \, dx \, dy \\
 [K_{r\varphi s1}^e] &= \int_0^a \int_0^b [B_{rs}]^T [D_{s\varphi1}] [B_\varphi] \, dx \, dy, [K_{r\varphi s3}^e] = \int_0^a \int_0^b [B_{rs}]^T [D_{s\varphi3}] [B_\varphi] \, dx \, dy, [K_{r\psi s1}^e] = \int_0^a \int_0^b [B_{rs}]^T [D_{s\psi1}] [B_\psi] \, dx \, dy, \\
 [K_{r\psi s3}^e] &= \int_0^a \int_0^b [B_{rs}]^T [D_{s\psi3}] [B_\psi] \, dx \, dy, \\
 [K_{rts1}^e] &= \int_0^a \int_0^b [B_{rs}]^T [D_{s1}] [B_{ts}] \, dx \, dy, [K_{rts3}^e] = \int_0^a \int_0^b [B_{rs}]^T [D_{s3}] [B_{ts}] \, dx \, dy, [K_{rtb2}^e] = \int_0^a \int_0^b [B_{rb}]^T [D_{b2}] [B_{tb}] \, dx \, dy
 \end{aligned}
 \tag{A-3}$$

The various rigidity matrices contributing to Eq. (A-3) can be denoted as follows:

$$\begin{aligned}
 [D_{b1}] &= \sum_{n=1}^N \int_{h_n}^{h_{n+1}} [C_b]^n dz, [D_{b2}] = \sum_{n=1}^N \int_{h_n}^{h_{n+1}} z[C_b]^n dz, [D_{b3}] = \sum_{n=1}^N \int_{h_n}^{h_{n+1}} z^2[C_b]^n dz \\
 [D_{b4}] &= \sum_{n=1}^N \int_{h_n}^{h_{n+1}} c_1 z^3 [C_b]^n dz, [D_{b5}] = \sum_{n=1}^N \int_{h_n}^{h_{n+1}} c_1 z^4 [C_b]^n dz, [D_{b7}] = \sum_{n=1}^N \int_{h_n}^{h_{n+1}} c_1^2 z^6 [C_b]^n dz \\
 [D_{b\phi 1}] &= \sum_{n=1}^N \int_{h_n}^{h_{n+1}} [e_b]^n dz, [D_{b\phi 2}] = \sum_{n=1}^N \int_{h_n}^{h_{n+1}} z[e_b]^n dz, [D_{b\phi 4}] = \sum_{n=1}^N \int_{h_n}^{h_{n+1}} c_1 z^3 [e_b]^n dz \\
 [D_{b\psi 1}] &= \sum_{n=1}^N \int_{h_n}^{h_{n+1}} [q_b]^n dz, [D_{b\psi 2}] = \sum_{n=1}^N \int_{h_n}^{h_{n+1}} z[q_b]^n dz, [D_{b\psi 4}] = \sum_{n=1}^N \int_{h_n}^{h_{n+1}} c_1 z^3 [q_b]^n dz [D_{s1}] = \sum_{n=1}^N \int_{h_n}^{h_{n+1}} [C_s]^n dz, \\
 [D_{s3}] &= \sum_{n=1}^N \int_{h_n}^{h_{n+1}} c_2 z^2 [C_s]^n dz, [D_{s5}] = \sum_{n=1}^N \int_{h_n}^{h_{n+1}} c_2^2 z^4 [C_s]^n dz, [D_{s\phi 1}] = \sum_{n=1}^N \int_{h_n}^{h_{n+1}} [e_s]^n dz, [D_{s\phi 3}] = \sum_{n=1}^N \int_{h_n}^{h_{n+1}} c_2 z^2 [e_s]^n dz, \\
 [D_{s\psi 1}] &= \sum_{n=1}^N \int_{h_n}^{h_{n+1}} [q_s]^n dz, [D_{s\psi 3}] = \sum_{n=1}^N \int_{h_n}^{h_{n+1}} c_2 z^2 [q_s]^n dz, [D_{\phi\phi}] = \sum_{n=1}^N \int_{h_n}^{h_{n+1}} [\eta]^n dz; [D_{\psi\psi}] = \sum_{n=1}^N \int_{h_n}^{h_{n+1}} [\mu]^n dz, \\
 [D_{\phi\psi}] &= \sum_{n=1}^N \int_{h_n}^{h_{n+1}} [m]^n dz
 \end{aligned} \tag{A-4}$$

Skew transformation

To incorporate skewed edges in the FE formulation and modify the stiffness matrices of the elements lying along the skewed edges transformation of the Cartesian co-ordinate axes along x', y'- and z'-directions is performed. The transformed DOFs pertaining to displacements can be shown as follows:

$$\{d_t\} = [T_t] \{d_t^1\}; \quad \{d_r\} = [T_r] \{d_r^1\}; \quad \{d_{r^*}\} = [T_{r^*}] \{d_{r^*}^1\} \tag{A-5}$$

The transformed stiffness and mass matrices can be represented as follows:

$$\begin{aligned}
 [\overline{K}_{tt}^e] &= [T_1]^T [K_{tt}^e] [T_1]; [\overline{K}_{tr}^e] = [T_1]^T [K_{tr}^e] [T_2]; [\overline{K}_{r^*r^*}^e] = [T_1]^T [K_{r^*r^*}^e] [T_2] \\
 [\overline{K}_{rr}^e] &= [T_2]^T [K_{rr}^e] [T_2]; [\overline{K}_{r^*r}^e] = [T_2]^T [K_{r^*r}^e] [T_1]; [\overline{K}_{r^*t}^e] = [T_2]^T [K_{r^*t}^e] [T_1]; [\overline{M}^e] = [T_1]^T [M^e] [T_1] [T_2];
 \end{aligned} \tag{A-6}$$

where $[T_1]$ and $[T_2]$ are banded transformation matrices with respect to skew angle λ and are given as:

$$[T_1] = \begin{bmatrix} \cos \lambda & \sin \lambda & 0 & -\sin \lambda \\ 0 & 0 & \cos \lambda & 0 \\ 0 & 0 & 0 & 1 \end{bmatrix}; [T_2] = [\cos \lambda \sin \lambda -\sin \lambda \cos \lambda] \tag{A-7}$$

Finally, Eq. (14) can be condensed to a more generalized form as follows:

$$[M_{tt}] \{\ddot{d}_t\} + [K_{eq}] \{d_t\} = 0 \tag{A-8}$$

where, $[K_{eq}]$ is the equivalent stiffness matrix.

Declaration of interest

None.

Data availability

The raw/processed data required to reproduce these findings cannot be shared at this time as the data also forms part of an ongoing study.

References

[1] Wang Z-X, Shen H-S. Nonlinear vibration of nanotube-reinforced composite plates in thermal environments. *Comput Mater Sci* 2011;50:2319–30.
 [2] Wang Z-X, Shen H-S. Nonlinear vibration and bending of sandwich plates with

- nanotube-reinforced composite face sheets. *Compos B Eng* 2012;43:411–21. <https://doi.org/10.1016/j.compositesb.2011.04.040>.
- [3] Kaci A, Tounsi A, Bakhti K, Adda Bedia EA. Nonlinear cylindrical bending of functionally graded carbon nanotube-reinforced composite plates. *Steel Compos Struct* 2012;12:491–504.
 - [4] Liew KM, Lei ZX, Zhang LW. Mechanical analysis of functionally graded carbon nanotube reinforced composites: a review. *Compos Struct* 2015;120:90–7.
 - [5] George N, Jeyaraj P, Murigendrappa SM. Buckling and free vibration of non-uniformly heated functionally graded carbon nanotube reinforced polymer composite plate. *Int J Struct Stabil Dynam* 2016;17:1750064.
 - [6] Selim BA, Zhang LW, Liew KM. Vibration analysis of CNT reinforced functionally graded composite plates in a thermal environment based on Reddy's higher-order shear deformation theory. *Compos Struct* 2016;156:276–90.
 - [7] Lei Z, Liew K, Yu J. Free vibration analysis of functionally graded carbon nanotube-reinforced composite plates using the element-free kp-Ritz method in thermal environment. *Compos Struct* 2013;106:128–38.
 - [8] Lei ZX, Zhang LW, Liew KM. Free vibration analysis of laminated FG-CNT reinforced composite rectangular plates using the kp-Ritz method. *Compos Struct* 2015;127:245–59.
 - [9] Kumar P, Srinivas J. Vibration, buckling and bending behavior of functionally graded multi-walled carbon nanotube reinforced polymer composite plates using the layer-wise formulation. *Compos Struct* 2017;177:158–70.
 - [10] Phung-Van P, Abdel-Wahab M, Liew KM, Bordas SPA, Nguyen-Xuan H. Iso-geometric analysis of functionally graded carbon nanotube-reinforced composite plates using higher-order shear deformation theory. *Compos Struct* 2015;123:137–49.
 - [11] Zhu P, Lei Z, Liew KM. Static and free vibration analyses of carbon nanotube-reinforced composite plates using finite element method with first order shear deformation plate theory. *Compos Struct* 2012;94(4):1450–60.
 - [12] Duc ND, et al. Static response and free vibration of functionally graded carbon nanotube-reinforced composite rectangular plates resting on Winkler-Pasternak elastic foundations. *Aero Sci Technol* 2017.
 - [13] Malekzadeh P, Zarei AR. Free vibration of quadrilateral laminated plates with carbon nanotube reinforced composite layers. *Thin-Walled Struct* 2014;82:221–32.
 - [14] Kiani Y. Free vibration of carbon nanotube reinforced composite plate on point supports using Lagrangian multipliers. *Meccanica* 2017;52:1353–67.
 - [15] Kiani Y. Free vibration of FG-CNT reinforced composite skew plates. *Aero Sci Technol* 2016;58:178–88.
 - [16] Mirzaei M, Kiani Y. Free vibration of functionally graded carbon-nanotube-reinforced composite plates with cutout. *Beilstein J Nanotechnol* 2016;7:511.
 - [17] Lin F, Xiang Y. Vibration of carbon nanotube reinforced composite beams based on the first and third order beam theories. *Appl Math Model* 2014;38:3741–54.
 - [18] Zhang LW, Lei ZX, Liew KM. Free vibration analysis of functionally graded carbon nanotube-reinforced composite triangular plates using the FSDT and element-free IMLS-Ritz method. *Compos Struct* 2015a;120:189–99.
 - [19] Zhang LW, Lei ZX, Liew KM. Vibration characteristic of moderately thick functionally graded carbon nanotube reinforced composite skew plates. *Compos Struct* 2015b;122:172–83.
 - [20] Fantuzzi N, Tornabene F, Bacciocchi M, Dimitri R. Free vibration analysis of arbitrarily shaped Functionally Graded Carbon Nanotube-reinforced plates. *Compos B Eng* 2017;115:384–408.
 - [21] Vinyas M, Sunny KK, Harursampath D, Trung NT, Loja MAR. Influence of interphase on the multi-physics coupled frequency of three phase smart magneto-electro-elastic composite plates. *Compos Struct* 2019;226:111254.
 - [22] Vinyas M, Nischith G, Loja MAR, Ebrahimi F, Duc ND. Numerical analysis of the vibration response of skew magneto-electro-elastic plates based on the higher-order shear deformation theory. *Compos Struct* 2019;214:132–42.
 - [23] Vinyas M. A higher order free vibration analysis of carbon nanotube-reinforced magneto-electro-elastic plates using finite element methods. *Compos B Eng* 2019;158:286–301.
 - [24] Vinyas M, Sandeep AS, Trung NT, Ebrahimi F, Duc ND. A finite element based assessment of free vibration behaviour of circular and annular magneto-electro-elastic plates using higher order shear deformation theory. *J Intell Mater Syst Struct* 2019. <https://doi.org/10.1177/1045389X19862386>.
 - [25] Vinyas M, Kattimani SC. Finite element evaluation of free vibration characteristics of magneto-electro-elastic rectangular plates in hygrothermal environment using higher-order shear deformation theory. *Compos Struct* 2018;202:1339–52.
 - [26] Vinyas M, Kattimani SC, Harursampath D, Nguyen Thoi-T. Coupled vibration of the free vibration characteristics of magneto-electro-elastic skew plates in hygrothermal environment. *Smart Struct Syst* 2019;24(2):267–92.
 - [27] Vinyas M, Harursampath D, Nguyen-Thoi Trung. A higher order coupled frequency characteristics study of smart magneto-electro-elastic composite plates with cut-outs using finite element method. *Defence Technology*; 2020. <https://doi.org/10.1016/j.dt.2020.02.009>.
 - [28] Vinyas M. On frequency response of porous functionally graded magneto-electro-elastic circular and annular plates with different electro-magnetic conditions using HSDT. *Compos Struct* 2020;240:112044.
 - [29] Natarajan S, Haboussi M, Manickam G. Application of higher-order structural theory to bending and free vibration analysis of sandwich plates with CNT reinforced composite facesheets. *Compos Struct* 2014;113:197–207.
 - [30] Mehar K, Panda SK, Dehngia A, Kar VR. Vibration analysis of functionally graded carbon nanotube reinforced composite plate in thermal environment. *J Sandw Struct Mater* 2016;18(2):151–73.
 - [31] Rabczuk T, Ren H, Zhuang X. A nonlocal operator method for partial differential equations with application to electromagnetics waveguide problem. *Comput Mater Continua (CMC)* 2019;59(1):31–55.
 - [32] Ren H, Zhuang X, Rabczuk T. A nonlocal operator method for solving partial differential equations. *Comput Methods Appl Mech Eng* 2020;358:112621. 2020.
 - [33] Ghasemi H, Park HS, Rabczuk T. A multi-material level set-based topology optimization of flexoelectric composites. *Comput Methods Appl Mech Eng* 2018;332:47–62.
 - [34] Ghasemi H, Park HS, Rabczuk T. A level-set based IGA formulation for topology optimization of flexoelectric materials. *Comput Methods Appl Mech Eng* 2017;313:239–58.
 - [35] Vu-Bac N, Duong TX, Lahmer T, Zhuang X, Sauer RA, Park HS, Rabczuk T. A NURBS-based inverse analysis for reconstruction of nonlinear deformations of thin shell structures. *Comput Methods Appl Mech Eng* 2018;331:427–55.
 - [36] Pan E, Han F. Exact solution for functionally graded and layered magneto-electro-elastic plates. *Int J Eng Sci* 2005;43(3–4):321–39.
 - [37] Ramirez F, Heyliger PR, Pan E. Discrete layer solution to free vibrations of Functionally Graded Magneto-Electro-Elastic plates. *Mech Adv Mater Struct* 2006;13(3):249–66.
 - [38] Huang DJ, Ding HJ, Chen WQ. Analytical solution for functionally graded magneto-electro-elastic plane beams. *Int J Eng Sci* 2007;45(2–8):467–85.
 - [39] Bhangale RK, Ganesan N. Free vibration of simply supported functionally graded and layered magneto-electro-elastic plates by finite element method. *J Sound Vib* 2006;294(4):1016–38.
 - [40] Milazzo A. A one-dimensional model for dynamic analysis of generally layered magneto-electro-elastic beams. *J Sound Vib* 2013;332(2):465–83.
 - [41] Milazzo A. Refined equivalent single layer formulations and finite elements for smart laminates free vibrations. *Compos B Eng* 2014;61:238–53.
 - [42] Feng WJ, Su RKL. Dynamic internal crack problem of a functionally graded magneto-electro-elastic strip. *Int J Solid Struct* 2006;43(17):5196–216.
 - [43] Vinyas M, Harursampath D, Trung NT. Influence of active constrained layer damping on the coupled vibration response of functionally graded magneto-electro-elastic plates with skewed edges. *Defence Technol* 2019. <https://doi.org/10.1016/j.dt.2019.11.016>.
 - [44] Vinyas M. Vibration control of skew magneto-electro-elastic plates using active constrained layer damping. *Compos Struct* 2019;208:600–17.
 - [45] Vinyas M, Kattimani SC. Finite element simulation of controlled frequency response of skewed multiphase magneto-electro-elastic plates. *J Intell Mater Syst Struct* 2019;30(12):1757–71.
 - [46] Vinyas M. Interphase effect on the controlled frequency response of three-phase smart magneto-electro-elastic plates embedded with active constrained layer damping: FE study. *Mater Res Express* 2020;6:125707.
 - [47] Hamdia KM, Ghasemi H, Zhuang X, Alajlan N, Rabczuk T. Sensitivity and uncertainty analysis for flexoelectric nanostructures. *Comput Methods Appl Mech Eng* 2018;337:95–109.
 - [48] Wu B, Yu JG, He CF. Wave propagation in non-homogeneous magneto-electro-elastic plates. *J Sound Vib* 2008;317(1–2):250–64.
 - [49] Wu CP, Tsai YH. Dynamic responses of functionally graded magneto-electro-elastic shells with closed-circuit surface conditions using the method of multiple scales. *Eur J Mech Solid* 2010;29(2):166–81.
 - [50] Hou PF, Leung AYT. The transient response of magneto-electro-elastic hollow cylinder. *Smart Mater Struct* 2004;13:762–76.
 - [51] Bhangale RK, Ganesan N. Free vibration studies of simply supported non-homogeneous functionally graded magneto-electro-elastic finite cylindrical shells. *J Sound Vib* 2005;288:412–22.
 - [52] Wu CP, Tsai YH. Static behavior of functionally graded magneto-electro-elastic shells under electric displacement and magnetic flux. *Int J Eng Sci* 2007;45:744–69.
 - [53] Li XY, Ding HJ, Chen WQ. Three-dimensional analytical solution for functionally graded magneto-electro-elastic circular plates subjected to uniform load. *Compos Struct* 2008;83:381–90.
 - [54] Sladek J, Sladek V, Krahulec S, Chen CS, Young DL. Analyses of circular magneto-electroelastic plates with functionally graded material properties. *Mech Adv Mater Struct* 2015;22:479–89.
 - [55] Vinyas M, Kattimani SC. Static studies of stepped functionally graded magneto-electro-elastic beam subjected to different thermal loads. *Compos Struct* 2017a;163:216–37.
 - [56] Vinyas M, Kattimani SC. Static analysis of stepped functionally graded magneto-electro-elastic plates in thermal environment: a finite element study. *Compos Struct* 2017b;178:63–85.
 - [57] Vinyas M, Kattimani SC. A Finite element based assessment of static behavior of multiphase magneto-electro-elastic beams under different thermal loading. *Struct Eng Mech* 2017c;62(5):519–35.
 - [58] Vinyas M, Kattimani SC. Hygrothermal coupling analysis of magneto-electroelastic beams using finite element methods. *J Therm Stresses* 2017d;41(8):1063–79.
 - [59] Vinyas M, Kattimani SC. Hygrothermal analysis of magneto-electro-elastic plate using 3D finite element analysis. *Compos Struct* 2017e;180:617–37.
 - [60] Vinyas M, Piyush JS, Kattimani SC. Influence of coupled fields on free vibration and static behaviour of functionally graded magneto-electro-thermo-elastic plate. *J Intell Mater Syst Struct* 2017;29(7):1430–55.
 - [61] Vinyas M, Kattimani SC. Static behavior of thermally loaded multilayered magneto-electro-elastic beam. *Struct Eng Mech* 2017;63(4):481–95.

- [62] Mohammadimehr M, Okhravi SV, AkhavanAlavi SM. Free vibration analysis of magneto-electro-elastic cylindrical composite panel reinforced by various distributions of CNTs with considering open and closed circuits boundary conditions based on FSDT. *J Vib Contr* 2018;24(8):1551–69.
- [63] Guo H, Zhuang X, Rabczuk T. A deep collocation method for the bending analysis of Kirchhoff plate. *Comput Mater Continua (CMC)* 2019;59(2):433–56.
- [64] Anitescu C, Atroshchenko E, Alajlan N, Rabczuk T. Artificial neural network methods for the solution of second order boundary value problems. *Comput Mater Continua (CMC)* 2019;59(1):345–59.
- [65] Samaniego E, Anitescu C, Goswami S, Nguyen-Thanh VM, Guo H, Hamdia K, Zhuang X, Rabczuk T. An energy approach to the solution of partial differential equations in computational mechanics via machine learning: concepts, implementation and applications. *Comput Methods Appl Mech Eng* 2020;362:112790.
- [66] Moita JMS, Soares CMM, Soares CAM. Analyses of magneto-electro-elastic plates using a higher order finite element model. *Compos Struct* 2009;91(4):421–6.
- [67] Kiran MC, Kattimani SC. Free vibration and static analysis of functionally graded skew magneto-electro-elastic plate. *Smart Struct Syst* 2018;21(4):493–519.